The nuclear basket regulates distribution and mobility of nuclear pore complexes in budding yeast

Janka Zsok[1], Francois Simon[2], Göksu Bayrak[1], Luljeta Isaki[1], Nina Kerff[2], Amy Wolstenholme[1] , Lucien E. Weiss[2]*, Elisa Dultz[1]*

[1]Institute of Biochemistry, ETH Zürich, 8093 Zürich
[2]Department of Engineering Physics, Polytechnique Montréal, Montréal, Québec, Canada

Abstract

Nuclear pore complexes (NPCs) mediate all traffic between the nucleus and the cytoplasm and are among the most stable protein assemblies in cells. Intriguingly, budding yeast cells carry two variants of NPCs which differ in the presence or absence of the nuclear basket proteins Mlp1, Mlp2 and Pml39. The binding of this basket structure is the last step of NPC assembly and Mlp-positive NPCs are excluded from the region of the nuclear envelope that is associated with the nucleolus. Here, we use recombination-induced tag exchange (RITE) to investigate the stability of all the NPC subcomplexes within individual NPCs. We show that the nuclear basket proteins Mlp1, Mlp2 and Pml39 remain stably associated with NPCs through multiple cell-division cycles. Mlp1/2 are responsible for the exclusion of NPCs from the nucleolar territory, but an independent pathway via Nup2 also contributes to the depletion of Mlp-negative NPCs from this region. We developed a method for single NPC tracking in budding yeast and observed that NPCs exhibit increased mobility in the absence nuclear basket components. Our data suggest that the distribution of NPCs on the nucleus is governed by the nuclear basket proteins and is the result of interactions with chromatin or chromatin-associated factors.

nuclear pore complex | Mlp1 | Nup2 | nuclear basket |
*Correspondence: elisa.dultz@bc.biol.ethz.ch & lucien.weiss@polymtl.ca

Introduction

Nuclear pore complexes (NPCs) are large macromolecular assemblies that stabilize pores in the nuclear envelope (NE) and mediate all macromolecular traffic between the nucleus and the cytoplasm in eukaryotic cells. NPCs are composed of multiple copies of approximately 30 different polypeptides termed nucleoporins (Nups). The core structure of the NPC consists of three rings, the inner ring in the centre of the NE, and the outer rings on either side of the NE (Figure 1A). Transmembrane Nups anchor the complex in the membrane. Central channel Nups containing phenylalanine-glycine (FG) repeats line the channel and mediate selective transport across the NE. In addition to these symmetric components, the nucleoplasmic and cytoplasmic faces of the NPC are decorated with asymmetric components, the cytoplasmic export platform and the nuclear basket.

Nuclear pore proteins are among the most stable proteins in multicellular organisms (D'Angelo & Hetzer, 2008; Toyama et al., 2019). In mammalian cells, the core of the NPC is stable throughout the entire cell cycle (Rabut et al., 2004) and can persist for weeks in non-dividing cells (Savas et al., 2012). In actively growing yeast cells, the half-life of many core nucleoporins exceeds several cell cycles in assembled NPCs (Hakhverdyan et al., 2021) and entire NPCs are inherited to daughter cells (reviewed in (Lusk & Colombi, 2014)).

It becomes increasingly clear that not all NPCs within a cell have the same composition (reviewed in (Dultz et al., 2022)). For example, components of the mRNA export machinery are lacking from NPCs in daughter cells, which delays the transition into S phase (Gomar-Alba et al., 2022) while replicatively aged yeast cells accumulate NPCs that lack components of the cytoplasmic export platform and the nuclear basket and contribute to ageing (Meinema et al., 2022). The study of such variant NPCs is severely limited by average-based bulk methods since they fail to capture the compositional heterogeneity in different complexes. Instead, methods that can distinguish between NPC subtypes and provide spatial and temporal resolution of single NPCs are required.

In exponentially growing budding yeast cells, the best described NPC variant are NPCs that lack the structural components of the nuclear basket (Bensidoun et al., 2022; Galy et al., 2004). The nuclear basket is composed of three highly dynamic Nups carrying FG or FXF(G) domains (Nup1, Nup60 and Nup2), and three structural Nups (Pml39, Mlp1 and Mlp2), here collectively referred to as the basket filaments (Figure 1B). The paralogues Mlp1 and Mlp2 are very large proteins with multiple interrupted coiled-coil regions that extend into the nucleoplasm (Strambio-de-Castillia et al., 1999). Nup60 recruits both Mlps as well as Nup2 to the nuclear basket via short binding sequences (Cibulka et al., 2022; Dilworth et al., 2001). Pml39 binds Mlp1 and to a lesser extend

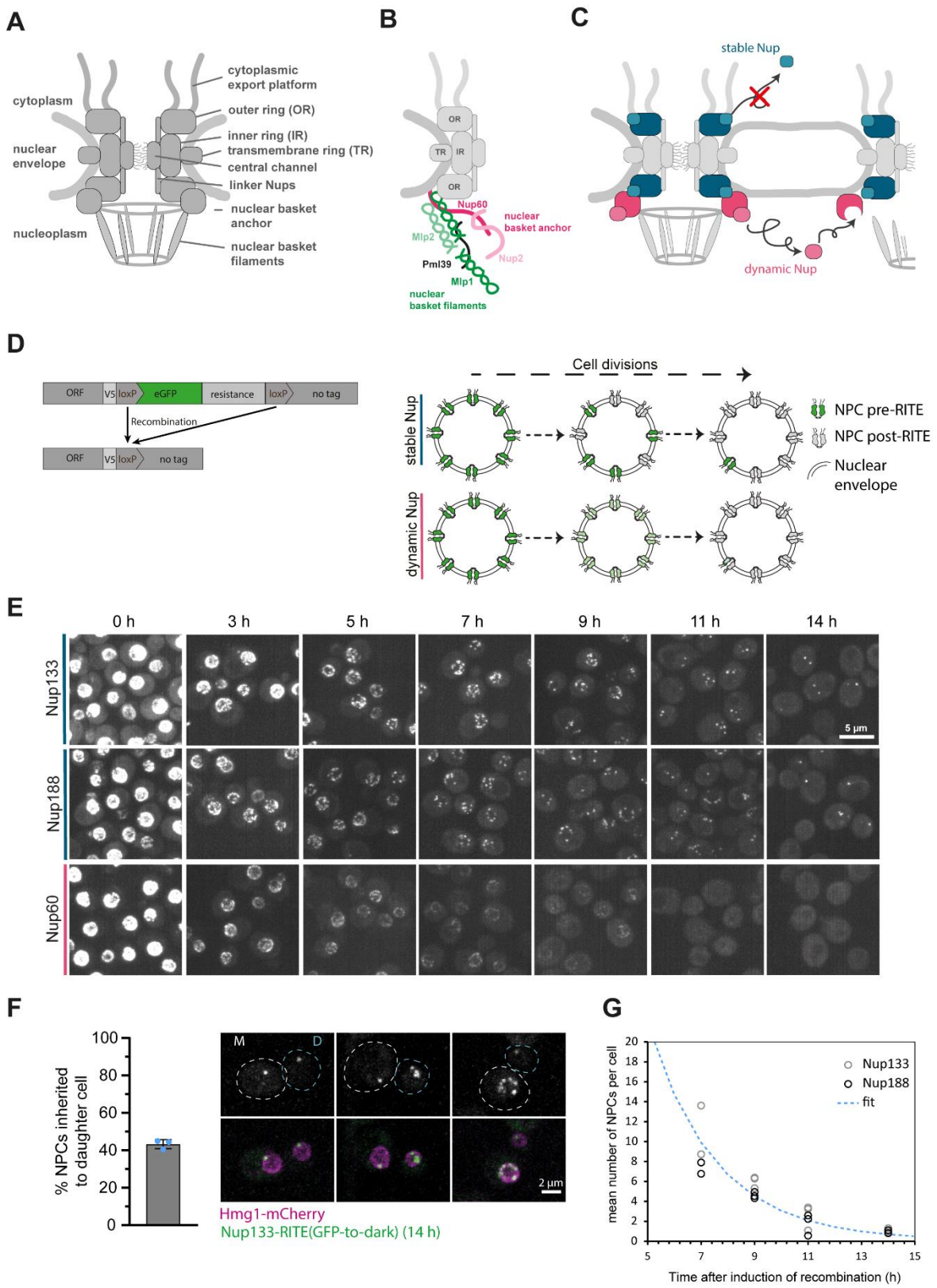

Figure 1: Single NPCs can be visualized using doRITE. (A) Overview of the subcomplexes in the NPC. **(B)** The organization of the nuclear basket. OR (outer ring), IR (inner ring), TR (transmembrane ring). **(C)** Behavior of a stable and a dynamic Nup. Stable Nups with a long residence half-life do not exchange with soluble subunits (blue). Dynamic Nups have a short residence half-life readily exchange with a soluble pool and between NPCs (magenta). **(D)** Left: Schematic of the RITE cassette to visualize old proteins. ORF: open reading frame; V5: V5-tag; loxP: loxP recombination site; eGFP: enhanced green fluorescent protein. Right: doRITE assay with a stable or dynamic Nup. **(E)** Exponentially growing cells expressing the indicated Nups endogenously tagged with a GFP-to-dark RITE cassette. Time stamps specify the time after induction of RITE. Maximum projections are shown. Colour bars represent membership to dynamic group in Figure 2A. **(F)** Inheritance pattern of NPCs from mother (M) to daughter (D) cells. Number of NPCs was counted in 100 M-D pairs with 1-14 pores per pair. Bar graph shows mean of three biological replicates (mean of individual replicates are shown as blue dots), error bar represents the standard deviation. Three examples of M-D pairs are shown as maximum projections. Hmg1-mCherry marks the NE. **(G)** Mean NPC numbers per cell determined from 100 cells per biological replicate at different time points after RITE(GFP-to-dark) induction for Nup133 or Nup188 (circles). The dashed line represents a fit of all shown datapoints with an exponential decay curve applying the experimentally determined doubling time of 1.75 h.

of Mlp1 to the NPC (Gunkel et al., 2023).

While Nup1, Nup60 and Nup2 are found on all NPCs, the nuclear basket filaments are present only on a subset (Bensidoun et al., 2022; Galy et al., 2004; Palancade et al., 2005). This may be the consequence of their extraordinary late assembly: they bind to the NPC on average ~40 min after all other Nups have assembled (Onischenko et al., 2020). The mechanism of this late assembly is unclear, but transcription inhibition and mutants in the 3' end polyadenylation and cleavage machinery of mRNA maturation were recently found to have defects in basket filaments assembly (Bensidoun et al., 2022). In wild type cells, mRNA export and processing factors are specifically enriched at NPCs with nuclear basket filaments, and the deletion of *PML39* or *MLP1* results in the leakage of unspliced RNAs into the cytoplasm (Galy et al., 2004; Palancade et al., 2005). This strongly implicates the nuclear basket filaments in a quality control step that regulates mRNA export. Mlp-positive NPCs are normally not found in the region of the NE adjacent to the nucleolus, which is devoid of mRNAs. Interestingly, in mutants that accumulate mRNAs in the nucleolus, Mlp-positive NPCs are no longer excluded from the nucleolar region (Bensidoun et al., 2022). There is thus an intricate relationship between the nuclear basket filaments and RNA maturation and export, but the exact mechanisms at play remain to be discovered.

In addition to being involved in mRNP quality control, the nuclear basket filaments also contribute to genome protection by supporting DNA repair pathways and preventing R loops (García-Benítez et al., 2017; Palancade et al., 2007). Intriguingly, a recent study showed that a role of the NPC in telomeric gene silencing is specifically fulfilled by NPCs without nuclear basket filaments (Kumar et al., 2023). NPCs with and without nuclear basket filaments thus carry out distinct specialized functions.

In this work, we develop recombination-induced tag exchange (RITE) into a system that allows us to track individual NPCs and to follow them through multiple cell cycles. We use this to systematically analyse the binding stability of Nups from all NPC subcomplexes in yeast. We show that Mlp1, Mlp2 and Pml39 are stably associated with NPCs through multiple cell cycles. Furthermore, we identify two pathways that reduce the density of NPCs in the nucleolar territory: First, binding of Mlp1/2 to mature NPCs prevents their localization in the nucleolar territory. Second, Nup2 leads to an increase of the residence time of all NPCs in the non-nucleolar territory possibly by mediating interactions with chromatin or chromatin-associated factors.

Results

doRITE allows the visualization of individual NPCs in living budding yeast cells

Live cell imaging of individual fluorescently tagged NPCs in budding yeast cells is severely limited by the high NPC density in the NE (~10 NPC/μm^2) (Winey et al., 1997). To enable the visualization of individual NPCs, we reduced the density of fluorescently labelled NPCs on the nucleus by recombination-induced tag exchange (RITE) (Verzijlbergen et al., 2009). In RITE, a protein tag is genomically exchanged through Cre-induced recombination, so proteins produced before or after recombination can be distinguished by their different tags (Figure 1D). Because core Nups remain associated with individual NPCs over hours or even days, RITE can be used to distinguish between old and new NPCs (Colombi et al., 2013; Onischenko et al., 2020; Toyama et al., 2019). We constructed a RITE-cassette that allows the switch from GFP-labelled protein to new protein that is not fluorescently labelled (RITE(GFP-to-dark)). We expected that successive cell divisions would dilute the labelled NPCs by inheritance to both mother and daughter cells if a stable Nup was tagged, while a dynamic Nup would not remain with individual NPCs but would instead redistribute to all NPCs of the nucleus (Figure 1C&D). We term this approach **d**ilution **o**f **RITE**-labelled complexes (doRITE). As a proof of concept, we performed doRITE on Nups previously reported to exhibit stable (Nup133, Nup188) or dynamic (Nup60) association with the NPC (Hakhverdyan et al., 2021; Onischenko et al., 2020; Rabut et al., 2004). We imaged the cells at different time points after the induction of recombination (Figure 1E). For Nup133 and Nup188, successive cell divisions led to the gradual dilution of fluorescent NPCs with only a few foci remaining after 6-7 divisions. In contrast, the signal of Nup60 gradually decreased on all NPCs until it became undetectable over background (Figure 1E). Since the turnover rate of Nup60 is similar to other Nups (Hakhverdyan et al., 2021), reduction of its signal in doRITE is unlikely to be caused by degradation. doRITE can thus distinguish between stable and dynamically associated Nups.

To determine whether the fluorescent foci observed in doRITE at late timepoints correspond to individual NPCs, we analysed their intensity and inheritance pattern. Nup133-GFP foci exhibited a narrow intensity distribution indicative of a single

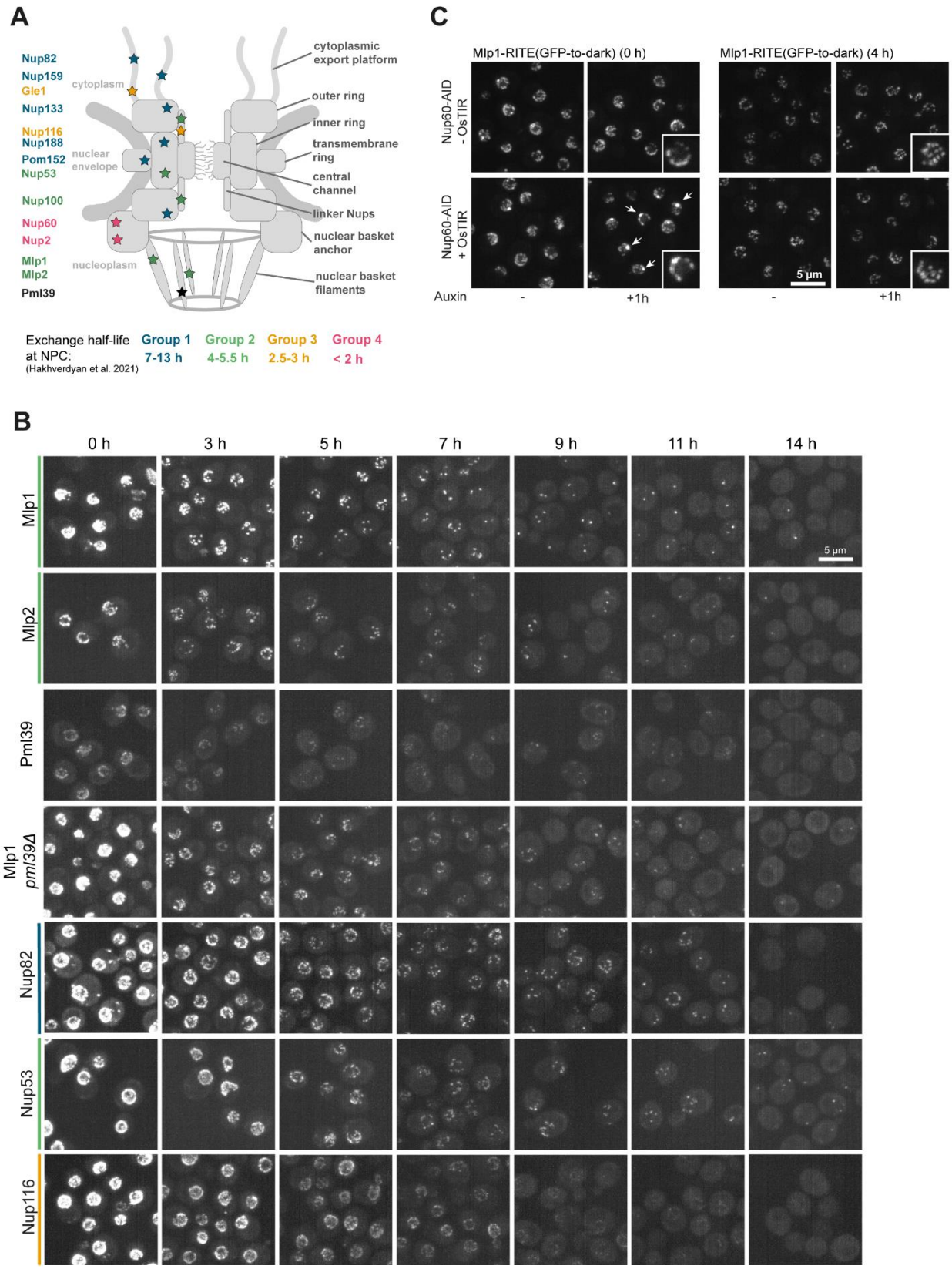

Figure 2: The Nups of the nuclear basket filaments Mlp1, Mlp2 and Pml39 are stably associated with the NPC. (A) Overview of the Nups analysed here. Approximate positions in the NPC are marked with stars. Colours correspond to the residence half-lives as characterized by Hakhverdyan et al., 2021. **(B)** Exponentially growing cells expressing the indicated Nups tagged with a GFP-to-dark RITE cassette. Time stamps specify time after induction of RITE. Maximum projections are shown. Colour bars represent membership to dynamic group in Figure 2A. **(C)** Cells expressing Nup60 tagged with an auxin-inducible degron (AID) in the absence or presence of the E3 ligase adaptor OsTIR1 were treated with auxin for 1 h. Arrows indicate Mlp1-GFP foci, which are not visible in Nup60-depleted cells that were induced for doRITE(GFP-to-dark) for four hours (right). Maximum projections are shown.

did not cluster at the spindle-pole body, as has been described for certain compromised NPCs ((Heath et al., 1995) Supplemental Figure S1B). Furthermore, they were inherited to daughter cells at a similar rate as bulk NPCs (43±2.4 (SD) %, Figure 1F, (Khmelinskii et al., 2010)). The average number of Nup133-RITE(GFP-to-dark) and Nup188-RITE(GFP-to-dark) foci per cell decayed exponentially (Figure 1G). By fitting this decay using the experimentally determined growth rate of the cells, we estimate an average of 158 ±22 (95% confidence interval) NPCs per cell at the time of recombination induction. This is at the upper end of the range expected in yeast cells (Winey et al., 1997), but the analysis likely overestimates the true number of NPCs because labelled Nups present in the soluble pool at the time of recombination continue to be incorporated and because we consider the induction of RITE as the timepoint 0 although recombination occurs asynchronously in the cell population.

In summary, our results strongly support the hypothesis that the observed foci represent individual NPCs. We conclude that doRITE can be used (1) to analyse the association dynamics of Nups at individual NPCs in vivo, (2) to follow the inheritance of individual NPCs from mother to daughter cell, and (3) to obtain single-NPC resolution in live cells with standard diffraction-limited microscopy.

Mlp1/2 and Pml39 associate with the NPC in a stable manner

Based on FRAP experiments, Mlp1 and Mlp2 were considered to exchange at the NPC within seconds (Niepel et al., 2013). However, a recent metabolic labelling-based biochemical analysis that systematically determined the exchange rate of all Nups on NPCs found the residence half-lives of Mlp1 and Mlp2 to be 4-5 hours (Hakhverdyan et al., 2021). To understand the function and regulation of the nuclear basket and to correctly interpret experimental results on (mis)localization phenotypes, it is crucial to know whether the basket filaments form a stable or dynamic assembly. Therefore, we performed doRITE with Mlp1 and Mlp2 to visualize their association dynamics with the NPC in living cells. For comparison, we also performed doRITE with a set of additional Nups from different NPC subcomplexes, which exhibited different dynamic behaviours by metabolic labelling (Hakhverdyan et al., 2021) (Figure 2A).

Mlp1, Mlp2 and Pml39 displayed similar behaviour to the stable Nups of group 1 (Nup133, Nup188, Pom152, Nup82, Nup159), which have an exchange half-life of greater than 7 hours at the NPC. Individual NPCs could clearly be distinguished for all of these Nups 14 h after induction of recombination (Figure 2B, Supplemental Figure S2A). In contrast, the analysed Nups of group 3, Nup116 (linker Nup) and Gle1 (cytoplasmic export platform), exhibited gradual reduction of the GFP-signal on all NPCs consistent with their dynamic association with the NPC (Figure 2B and Supplemental Figure S2A). Thus, Mlp1, Mlp2 and Pml39 associate stably with NPCs over multiple generations, although we cannot exclude the existence of an additional more dynamic pool of these proteins which could not be visualized by doRITE.

Pml39 was recently shown to anchor a subpopulation of Mlp1 to the NPC (Gunkel et al., 2023). To test whether Pml39 is required for the assembly of stable nuclear basket filaments, we performed doRITE with Nup133 and Mlp1 in *pml39*⊿ cells. Deletion of *PML39* had no effect on the dynamics of Nup133 (Figure S3A). Mlp1-RITE(GFP-to-dark) still formed the characteristic NPC-foci after 14 hours of recombination in the absence of Pml39, but their intensity was reduced compared to wild type cells (Figure 2B). This is consistent with the presence of a Pml39-dependent subpopulation of Mlp1 at the 14h-old NPCs but indicates that Pml39 is not necessary to form stable basket filaments.

Although Nup60 is essential for the recruitment of Mlp1/2 to the NPC, it was recently shown to be dispensable for maintenance of already assembled Mlp1/2 at the NPC in meiotic cells (King et al., 2023). We tested whether this is also the case in exponentially growing cells. Indeed, we observe that depletion of Nup60 via an auxin-inducible degron tag (Nishimura et al., 2009) did not affect the localization of Mlp1-RITE(GFP-to-dark) four hours after induction of RITE, suggesting that old Mlp1 protein was maintained at NPCs (Figure 2C). In contrast, when all Mlp1 was labelled (no induction of RITE), a fraction of Mlp1-GFP accumulated in a nuclear focus reminiscent of the Mlp1-GFP focus formed in *nup60*⊿ cells (Feuerbach et al., 2002; Niepel et al., 2013) (Figure 2C). Since this focus is not visible, when only old protein is labelled, it is composed of newly synthesized protein that is not incorporated into the NPC in the absence of Nup60. Thus, Nup60 is required for the assembly of Mlp1 into the NPC but not for its maintenance. This appears to be an evolutionary conserved mechanism as it was also reported for the human homologues Nup153 and TPR (Aksenova et al., 2020).

Exclusion of old NPCs from the nucleolar territory is mediated by Mlp1/2

It has been proposed that the nucleolar environment prevents the assembly of nuclear basket filaments and for that reason Mlp positive NPCs are not found in this region of the NE. However, since we showed that nuclear basket filaments are stable for several hours, the absence of Mlp-positive NPCs from the nucleolar territory is more likely due to the lack of lateral movement of Mlp-positive NPCs into this region. To shed further light on the molecular mechanism of nucleolar exclusion, we first wanted to test whether this is mediated entirely by Mlp1/2 or whether other factors are involved. Since the integration of Mlp1 and Mlp2 into the NPC occurs on average within one hour of assembly (Onischenko et al., 2020), we expected that the NPCs visualized as individual foci by doRITE at the 14-hour timepoint would all carry Mlp1/2 and thus be excluded from the nucleolar territory. Indeed, only 5.2 ±1 % of 14 h-old Nup133-RITE(GFP-to-dark) NPCs were detected in the nucleolar territory marked by Nop1-RFP. Deletion of *MLP2* did not significantly change this, but in *mlp1Δ* and *mlp1Δ mlp2Δ* cells the fraction of 14-hour old NPCs detected in the nucleolar territory increased to 17.9 ±4 % and 15.6 ±3 %, respectively (Figure 3A). Importantly, overall NPC stability was not affected by mutations in basket proteins as observed by doRITE with Nup133-RITE(GFP-to-dark) (Supplemental Figure S3A). Our result suggests that Mlp1 alone is sufficient to mediate nucleolar exclusion. However, the fraction of 14-hours old NPCs in the nucleolar territory in *mlp1Δ mlp2Δ* cells was still lower than expected from a random distribution, since the nucleolar territory occupies approximately 30 % of the nuclear surface (Berger 2008). Since newly assembled NPCs also lack Mlp1 and Mlp2, we tested whether they exhibit a similar distribution. We used an inverted RITE cassette (dark-to-GFP) to visualize newly assembled NPCs (Supplemental Figure S3B). Nup133-RITE(dark-to-GFP) generated a more diffuse NE signal at early timepoints that made the identification of individual newly assembled NPCs difficult – possibly due to the interaction of Nup133 with the membrane via an amphipathic helix (Nordeen et al., 2020). We therefore used Nup188 to compare the fraction of old (GFP-to-dark at 14 h) and new (dark-to-GFP at 45 min) NPCs in the nucleolar territory. 5.6 ±0.4 % of 14-hour old NPCs were detected in the nucleolar territory, in contrast to 14.2 ±1.4 % of newly assembled NPCs (Figure 3B). This closely recapitulates the fraction of 14-hour old NPCs observed in the nucleolar territory in wildtype versus *mlp1Δ mlp2Δ* cells and demonstrates that in the absence of Mlp1/2, 14 h-old NPCs behave like newly assembled NPCs with respect to their nucleolar localization. The distribution still differed from a random distribution, and we follow up on this below.

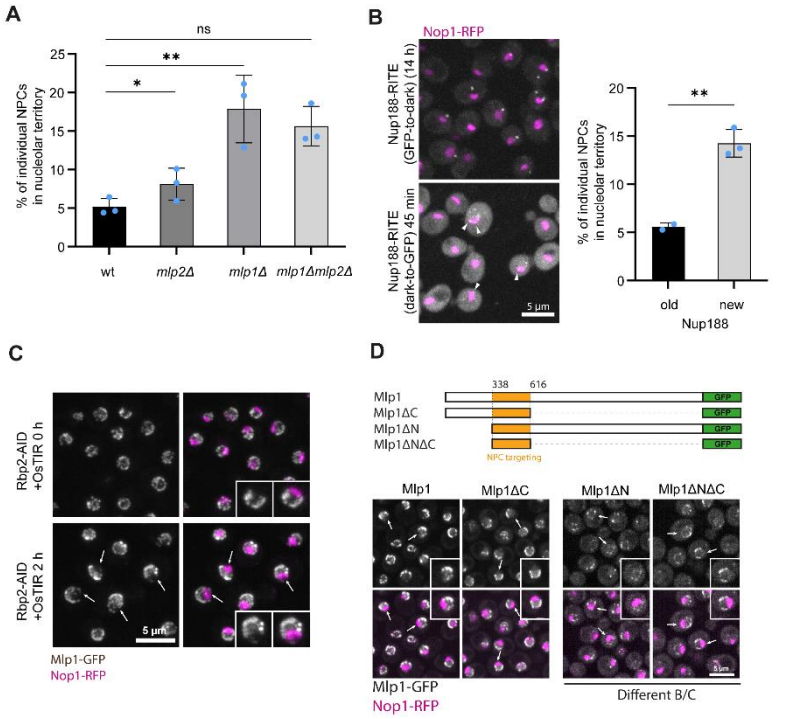

Figure 3: Exclusion of old NPCs from the nucleolar territory depends on Mlp1. **(A)** Nup133-RITE(GFP-to-dark) in wild type and indicated mutants was induced for doRITE for 14 h. At least 50 cells were analyzed per condition and replicate by scoring the localization of NPCs in- or outside the nucleolar territory marked by Nop1-RFP. Blue dots show means of individual biological replicates and error bars the standard deviation. Stars indicate significance in one-way ANOVA with Sidak multiple comparison correction: * p<0.05, ** p<0.005, ns not significant. **(B)** Exponentially growing cells labelled with Nup188-GFP-to-dark (old) and Nup188-dark-to-GFP (new), were induced for 14 h and 45 min, respectively. At least 70 cells were analysed by scoring the localization of NPCs in- or outside the nucleolar territory marked by Nop1-RFP. Image panels show maximum projections. Arrowheads point to new NPCs in the nucleolar territory. Blue dots show means of individual biological replicates and error bars the standard deviation. Stars indicate significance in unpaired t-test: ** p<0.005. **(C)** Exponentially growing cells expressing Mlp1-GFP and carrying the auxin inducible degron system on polymerase II subunit Rbp2 were induced for auxin-induced degradation for 2 hours. Arrows mark nucleoli with clear lack of Mlp1-GFP signal. Maximum projections are shown. **(D)** Mlp1 truncations (top) and their localization upon expression in cells (bottom). The truncations were introduced into a *mlp1Δ* background. All truncations are depleted from nucleolar territory (arrows). Due to low expression of the constructs lacking the N-terminus, the right panels are adjusted with different brightness and contrast settings (Different B/C). Maximum projections are shown.

The exclusion of Mlp1-positive NPCs from the nucleolar territory could be due to their retention in the non-nucleolar territory, e.g. via their interactions with nascent mRNA and mRNA maturation factors (Bensidoun et al., 2022; Bermejo et al., 2011; Saroufim et al., 2015). To test whether transcription affects nucleolar exclusion, we analysed Mlp1-GFP labelled NPCs in cells with an auxin-inducible degron tag on the Rpb2 subunit of Polymerase II (Pol II) (Patrizia Derrer et al., 2019). As reported in Bensidoun et al. (2023), we observed an increase in the nucleoplasmic signal of Mlp1 upon depletion of Pol II (Figure 3C). However, Mlp1-containing NPCs remained excluded from the nucleolar territory (Figure 3C). Thus, although inhibition of transcription plays a role in nuclear basket assembly, the exclusion of Mlp1-containing NPCs from the nucleolus is maintained.

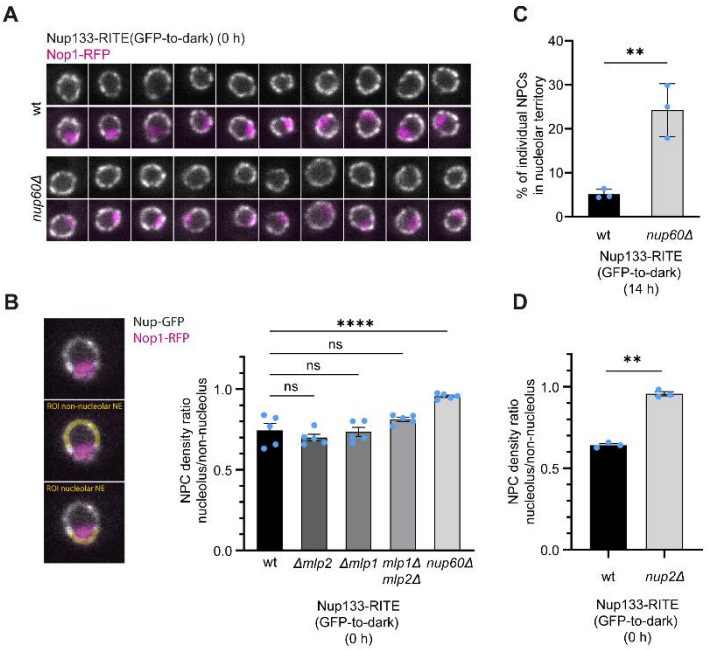

Figure 4: Exclusion of newly assembled NPCs from the nucleolar territory is mediated by Nup2. **(A)** Representative nuclei of exponentially growing wild type and *nup60Δ* cells expressing Nup133-RITE(GFP-to-dark) and Nop1-RFP. Cells were imaged without induction of recombination. **(B)** Left: Example of regions of interest (ROIs) used to quantify Nup-GFP-intensity in the nucleolar and non-nucleolar region of the NE. Right: Mean ratio of Nup133-RITE(GFP-to-dark) in the nucleolar versus non-nucleolar territory without induction of recombination for wild type and nuclear basket deletion mutants. Blue dots show mean of biological replicates and error bars the standard deviation. At least 50 cells were analysed per replicate and condition. Stars indicate significance in one-way ANOVA with Sidak multiple comparison correction: **** p<0.0001, ns not significant. **(C)** Nup133(GFP-to-dark) in wild type and *nup60Δ* cells were induced in doRITE for 14 h. At least 50 cells were analyzed per condition and replicate by scoring the localization of NPCs in- or outside the nucleolar territory marked by Nop1-RFP. Blue dots show means of individual biological replicates and error bars the standard error of the mean. Stars indicate significance in unpaired t-test: ** p<0.005. **(D)** Mean ratio of Nup133-RITE(GFP-to-dark) in the nucleolar versus non-nucleolar territory without induction of recombination for wild type and *nup2Δ* cells. Blue dots show mean of biological replicates and error bars the standard error of mean. At least 50 cells were analysed per replicate and condition. Stars indicate significance in unpaired t-test: ** p<0.005.

The NPC-binding domain of Mlp1 exhibits preference for the non-nucleolar territory

Next, we wanted to test which domain of Mlp1 mediates the exclusion from the nucleolus. A domain encompassing amino acids 338-616 of Mlp1 mediates localization to the NPC via binding to Nup60 and was reported to localize homogeneously to all NPCs (Cibulka et al., 2022; Niepel et al., 2013). We truncated the endogenous Mlp1 gene to express this NPC binding fragment alone (ΔNΔC) or with the endogenous N- or C-terminal part of Mlp1 fused to GFP (Schematic representation Figure 3D). All three fragments were excluded from the nucleolar territory (Figure 3D). The lower NE signal observed especially for Mlp1(ΔN)-GFP and Mlp1(ΔNΔC)-GFP could be partially due to the failure to recruit Pml39 and therefore additional copies of Mlp1-GFP but also due to overall reduced expression or enhanced degradation rates. Mlp1(ΔNΔC)-GFP exhibited similar exclusion from the nucleolar territory when expressed from a CEN plasmid in *mlp1⊿mlp2⊿* cells (Supplemental Figure S3D). However, in rare, highly expressing cells, Mlp1(ΔNΔC)-GFP was also found in the nucleolar territory as reported previously (Niepel 2013, Supplemental Figure S3D). This could indicate that the fragment prefers NPCs in the non-nucleolar territory but can in principle also access the nucleolar territory as suggested recently for the full length Mlp1 protein (Bensidoun et al., 2022).

Nup2 restricts the localization of NPCs to the nucleolar territory independent of their age

Approximately 30 % of the NPCs would be expected to localize to the nucleolar territory if they were randomly distributed, but we only detected 14.2 ±1.4 % of the newly assembled NPCs there (Figure 3B). This suggests that an additional, Mlp-independent mechanism must be involved in restricting the localization of NPCs to the nucleolar territory. Indeed, a reduced density of NPCs in the nucleolar territory was previously observed (Wang et al., 2016). To test whether the nuclear basket contributes to this, we quantified the NPC density in the nucleolar and non-nucleolar territory in basket deletion mutants. In a strain expressing Nup133-RITE(GFP-to-dark) without RITE induction, where all NPCs are labelled, the mean NPC density in the nucleolar territory was 74 ±4 % of that in the non-nucleolar territory in wild type cells (Figure 4B).

However, deletion of *NUP60* led to a homogenous distribution of the NPCs around the entire nucleus and the density ratio of the nucleolar vs. non-nucleolar territory was close to 1 (0.95 ±0.01 (SEM)) (Figure 4A+B). Similarly, the fraction of 14 h-old NPCs detected in the nucleolar territory increased to 24 ±6 % in *nup60⊿* cells (Figure 4C) supporting a random, homogeneous distribution of NPCs. Furthermore, auxin-mediated depletion of Nup60 led to an increased NPC density in the nucleolar territory (Supplemental figure S4A+B), while Mlp1-containing NPCs remained excluded from the nucleolar territory (Figure 2C).

Since deletion of *MLP1* and *MLP2* individually or in combination did not affect the density ratio (Figure 4B), our results suggest that Nup60 reduces the density of NPCs in the nucleolar territory via an Mlp1/2 independent mechanism. Since Nup60 additionally recruits Nup2 (Dilworth 2001), we measured NPC density in the nucleolar territory in *nup2⊿* cells. In these cells, the localization of Mlp1 to NPCs is not affected (Galy et al., 2004). Like *nup60⊿* cells, *nup2⊿* cells exhibited a homogeneous distribution of NPCs over the entire NE (Figure 4D). Since Mlp1-positive NPCs remain excluded from the nucleolar territory in *nup2⊿* cells (Galy et al., 2004), the homogenous distribution observed in this mutant must be caused predominantly by the redistribution of Mlp-negative NPCs into the nucleolar territory.

Taken together, we conclude that two independent molecular mechanisms lead to a reduced NPC density in the nucleolar territory. First, NPCs become depleted from the nucleolar territory once they bind the nuclear basket proteins Mlp1/2. Second, Nup2 contributes to the exclusion of all NPCs from the nucleolar territory.

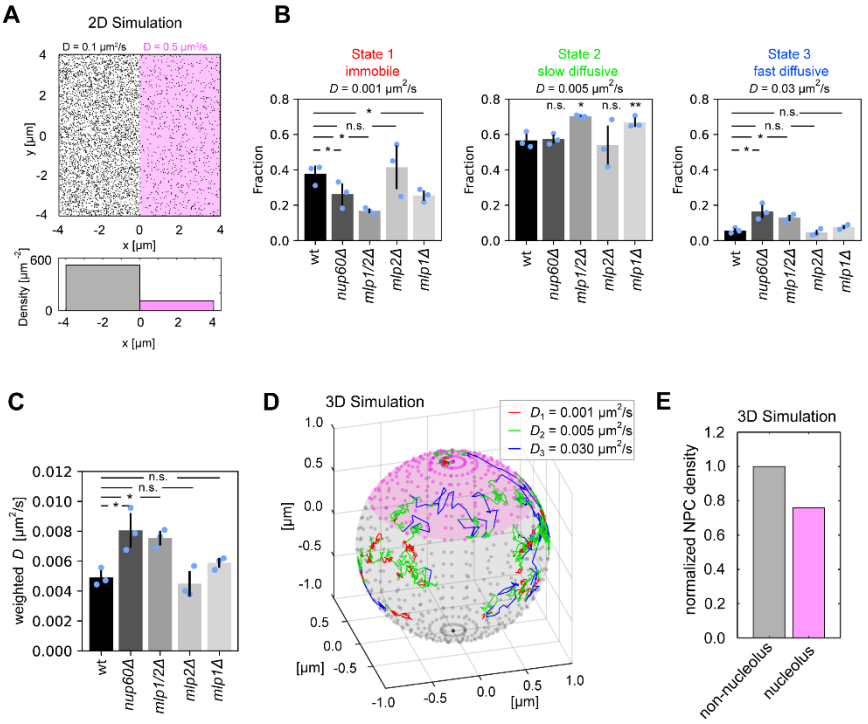

Figure 5: The nuclear basket proteins influence the mobility of NPCs. (A) 2D simulation of 1000 particles diffusing for 2000 timesteps in two territories with different diffusion coefficients as indicated (positions in the final time point are shown). The bar graph in the bottom shows the densities of the particles found in each area at the end of the simulation. **(B)** Tracks of NPCs labelled with Nup133-RITE(GFP-to-dark) obtained 14 hours after RITE induction from cells carrying the indicated gene deletions were analysed with a 3-state model (Immobile, slow diffusive and faster diffusive) with fixed diffusion coefficients as indicated. Bar graphs display the fraction of particles in each state computed from the transition rates between states. Results from individual biological replicates are shown as blue dots, the error bars represent the standard deviation of the three replicates. Stars indicate significance in pairwise t-tests comparing each mutant to the wild type: * p<0.05, ** p<0.01, ns not significant. At least 1100 tracks were analysed per condition and replicate. **(C)** Average diffusion coefficients derived from data displayed in **(B)** by weighting the three diffusion coefficients according to their respective fractions. The error bars represent the standard deviation. Stars indicate significance in pairwise t-tests comparing each mutant to the wild type: * p<0.05, ns not significant. **(D)** Simulation of particles diffusing on a sphere with three movement states. In the grey area, which represents the non-nucleolar territory, particles transition between states according to the rates extracted from tracking data in the wild type cells, while transition rates in the pink area, which represent the nucleolar territory, correspond to the ones from *nup60Δ* cells (Figure S5C). Three example tracks are shown and coloured according to the state the particle occupies in each timestep. **(E)** Steady state particle density in the nucleolar region relative to the density in the non-nucleolar regions obtained from the simulation

Basket components affect the mobility of NPCs in the NE

The partial depletion of NPCs from the nucleolar territory could be caused by a barrier that inhibits entry or by interactions that prolong the time spent in the non-nucleolar territory. We consider the second option more plausible, since the nuclear basket is known to interact with multiple binding partners in the chromatin region (reviewed in (Sumner & Brickner, 2022)). More interactions in the non-nucleolar territory should manifest in a lower mobility of the NPCs in this region. We applied simulations and tracking of individual NPCs in the NE to test this idea.

First, we confirmed in a 2D simulation that a local decrease in the diffusion rate indeed causes a local increase in particle density (Figure 5A). Next, we compared the diffusion of Nup133-RITE(GFP-to-

dark)-labelled NPCs 14 h after induction of recombination in wild type cells with that in different nuclear basket deletion mutants (*nup60⊿*, *mlp1⊿*, *mlp2⊿* and *mlp1⊿/2⊿)*. In wild type cells, we expect these 14 h-old NPCs to be predominantly Mlp-positive and their mobility therefore influenced by interactors of Mlp1/2 as well as Nup2 in the non-nucleolar region. In contrast, in *nup60⊿* cells, we observed homogenous distribution of NPCs suggesting abrogation of all diffusion differences in the nucleolar and non-nucleolar territory. Therefore, the measured movement of 14 h-old NPCs in *nup60⊿* cells could represent the behaviour of NPCs in the nucleolar territory. We tracked and analysed the NPC movement with our probabilistic method, ExTrack (Simon et al., 2023). In wild type cells, NPC mobility exhibited behaviour switching between immobile, slow diffusive, and fast diffusive states (states 1, 2, & 3, Figure 5B, Supplementary Figure S5A). The diffusion coefficients of these states were similar in all analysed strains (Supplementary Figure S5B), but we detected changes in the fractions of NPCs that occupied the different diffusion states (Figure 5B). NPCs in *mlp1⊿ mlp2⊿* double mutants and *nup60⊿* mutants spend more time in the fast diffusive state relative to the WT. This population shift translates into an overall increase in the average diffusion coefficients of these strains, where *mlp1⊿ mlp2⊿* and *nup60⊿* had average diffusion coefficient that were 63 ±8 % and 53 ±14 % higher than the wildtype, respectively (Figure 5C). This is consistent with previous FRAP experiments that showed increased mobility of NPCs in *mlp1⊿ mlp2⊿* cells (Niepel et al., 2013; Spichal et al., 2016). To test if this change in the movement behaviour could explain the changes in NPC distribution, we constructed a 3D diffusion model, where NPCs diffuse on a spherical nucleus with different diffusion characteristics in a cap region representing the nucleolar territory (Figure 5D). We applied the diffusion parameters from wild type cells in the non-nucleolar territory and those from *nup60⊿* cells in the nucleolar territory (Figure 5D, see Track Simulations in the Methods). Our simulation suggests that at steady state, the density of NPCs in the nucleolar territory would be 76 ±3 % of that in the non-nucleolar territory, which closely replicates our experimental result (74 ±4 % in wild type cells, compare Figure 5E to Figure 4B).

Our data and simulation thus support the hypothesis that an increased apparent diffusion coefficient is responsible for the reduced NPC density in the nucleolar territory (Figure 5A, D&E). Indeed, the tracks from *mlp1⊿mlp2⊿ and nup60⊿* cells exhibit a reduced frequency of binding events, that is less transitions from a diffusive to a bound state (Supplementary Figure S5C). This would be consistent with reduced interactions of NPCs with nuclear components in these strains. However, since the two mutants exhibit similar average diffusion coefficients (Figure 5C), the observed difference in mobility can probably be attributed to the loss of Mlp1/2 only, which is absent in both mutants. This interpretation is corroborated by the observation that acute depletion of Nup60, which does not affect the localization of Mlp1, did not affect NPC mobility (Supplemental Figure S5D). Thus, our results support the hypothesis that the NPC distribution can be the result of differential interactions in the different regions of the nucleus (Figure 6), but at this point we cannot tease apart the Mlp-dependent and -independent roles of Nup60 in this process.

Discussion

doRITE as a versatile tool for single NPC analysis in yeast

To understand the differences between NPC variants, it is crucial to develop methods that do not only report on bulk behaviour but can distinguish between subpopulations of NPCs and ideally provide single NPC resolution. While the resolution of single NPCs can readily be achieved by confocal microscopy on the flat bottom of many adherent mammalian cell types, it poses a greater challenge on the small spherical yeast nucleus with its high NPC density. With doRITE (Figure 1D-E) we developed a versatile tool to achieve single NPC resolution in *S. cerevisiae* by utilizing the unique properties of NPCs: (i) high stability of the complex, (ii) multiple copies of the labelled protein per complex, and (iii) intact inheritance through multiple cell cycles. In this work, we have harnessed doRITE to analyse the exchange dynamics of different Nups at the NPC (Figure 2), to determine the localization of single NPCs relative to nuclear landmarks (Figure S1B, 3&4) and to track the movement of NPCs in the NE (Figure 5). In the future, the tracking and analysis pipeline we developed will be applicable to further study the forces that act on NPCs and drive their movement and distribution on the nucleus. doRITE could in principle also be applied to other stable complexes such as the ribosome, but the NPC is particularly suitable due to the presence of several copies of the labelled protein per complex which yields a high signal-to-noise ratio.

The nuclear basket filaments form a stable structure on the NPC

FRAP is a common method to investigate the dynamics of biological molecules and was used to

characterize Nup dynamics in mammalian cells systematically (Rabut et al., 2004). However, only highly dynamic interactions at NPCs, like those of transport receptors, can be quantified by FRAP in budding yeast (Patrizia Derrer et al., 2019), since longer measurements are confounded by the mobility of entire NPCs on the nuclear surface. doRITE overcomes this limitation and provides a complementation to biochemical assays, which were recently used to determine the exchange rate of Nups on the NPC (Hakhverdyan et al., 2021; Onischenko et al., 2020).

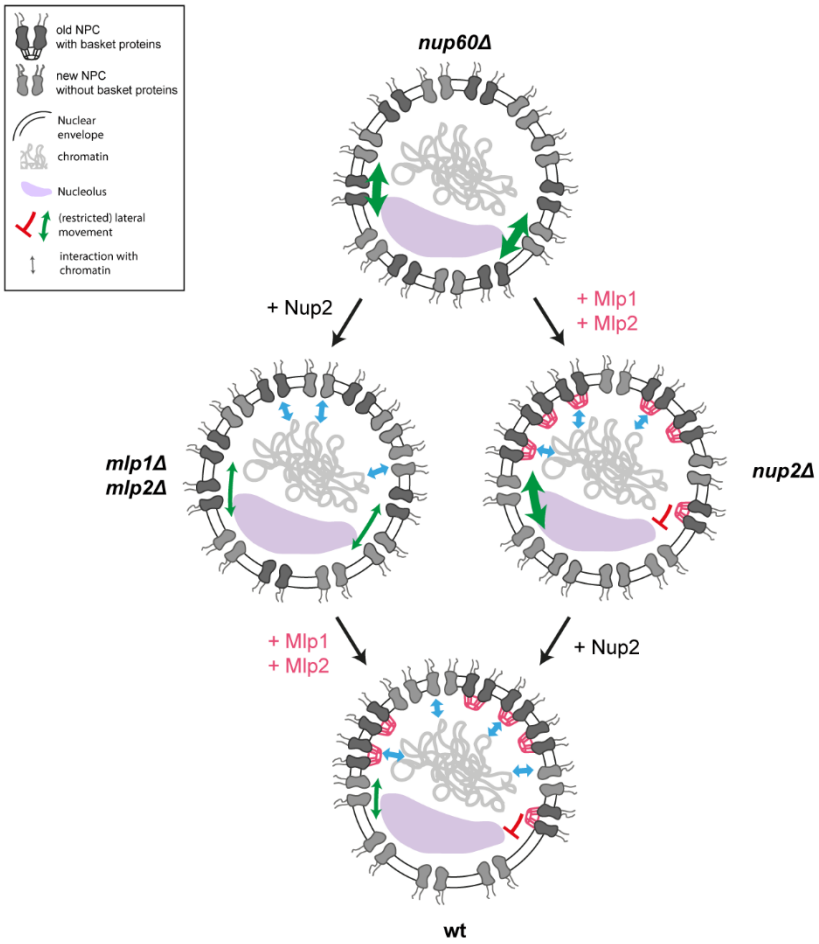

Figure 6: Model of two independent pathways that regulate distribution and movement of NPCs on the nucleus

Our results are largely in agreement with the previously reported overall categorisation of Nups into stable and dynamic based on biochemical data (Figure 2, (Hakhverdyan et al., 2021)). However, we observed that the Nups from group 2 (Mlp1, Mlp2, Nup53 and Nup100) with residence times at the NPC of 4.5-5 hours exhibit stable properties in our doRITE assay similar to the stable core Nups of group 1 (Figure 2B). This discrepancy could arise from the presence of two pools with different dynamic behaviour, of which the mass-spectrometry approach would observe the average while our doRITE approach would primarily visualize the more stable pool. The interpretation of Mlp1 as a stable Nup is corroborated by the observation that - once assembled - it is maintained at the NPC independent of Nup60 (Figure 2C), as also reported for meiotic budding yeast and mammalian cells (Aksenova et al., 2020; King et al., 2023). Interestingly, Mlp1 also forms stable assemblies at the NPC when *PML39* is deleted (Figure 2C), suggesting that the additional copies of Mlp1 recruited to the NPC by Pml39 (Gunkel et al., 2023) are not required for assembly of stable nuclear basket filaments. Although we present clear evidence for the stable assembly formed by Mlp1, Mlp2 and Pml39 on the nucleoplasmic face of the NPC, we cannot exclude that a second more mobile pool exists which might be associated with the NE more generally as suggested by labelling at NE sites away from the NPCs by immuno-gold (Strambio-de-Castillia et al., 1999). Furthermore, transient interactions via Nup60 could prevail during early assembly stages that are converted into more stable interactions only during maturation of the nuclear basket.

NPC retention in the non-nucleolar territory of the NE is mediated by the basket proteins Mlp1/2 and Nup2

Our work identifies two independent mechanisms that contribute to the preference of NPCs for the non-nucleolar territory, one specific for Mlp-positive NPCs and one that affects all NPCs (Model Figure 6).

As previously observed, Mlp-positive NPCs are excluded from the nucleolar territory (Galy et al., 2004; Niepel et al., 2005). In agreement with the delayed assembly of Mlp1/2 into NPCs, we show that nucleolar depletion mediated by Mlp1/2 is specific to old NPCs (Figure 3A&B). It is unclear what molecular mechanisms mediate the exclusion of Mlp-positive NPCs from the nucleolar territory. We consider two hypotheses: retention in the non-nucleolar region due to interaction with chromatin (Figure 6, blue arrow) or a barrier that prevents entry of Mlp-positive NPCs into the nucleolus (Figure 6, red inhibition signal). By analysing truncation

mutants, we find that even the minimal characterized NPC binding domain of Mlp1 (Cibulka et al., 2022; Niepel et al., 2013) exhibits a preference for NPCs in the non-nucleolar territory (Figure 3D). However, it appears that this domain, and also the full length Mlp1 protein, in principle have access to the nucleolus ((Bensidoun et al., 2022) , Figure S3D). Thus, nucleolar exclusion might be mediated only in the context of the assembled basket. We tested whether tethering through mRNA interactions could be involved, however, nucleolar exclusion of Mlp-positive NPCs was maintained upon depletion of Pol II (Figure 3C), suggesting that the mechanism does not rely on mRNA itself. Alternatively, exclusion could be mediated by the specific biophysical properties of the nucleolus (reviewed in (Tartakoff et al., 2022)).

In addition, we describe an Mlp-independent mechanism that leads to a reduced density of NPCs in the nucleolar territory and relies on Nup2 (Figure 4D). Nup2 and its homologues in *Aspergillus nidulans* and metazoa have been shown to interact with chromatin (Holzer et al., 2021; Ishii et al., 2002; Markossian et al., 2015), which could lead to the preferred localization of NPCs bound by Nup2 to the non-nucleolar region of the NE, since chromatin is apart from the rDNA locus largely absent from the nucleolus. Our tracking analysis overall supports the hypothesis that the modulation of diffusion due to differential interactions can lead to a non-homogeneous distribution of NPCs on the NE (Figure 5).

In summary, our study contributes a versatile tool for the analysis of NPCs in living cells. We use this to better understand the properties and organization of the nuclear basket. However, many questions regarding the regulation of its assembly and its functional role at the NPC remain to be answered in the future.

Materials and Methods

Yeast strain and plasmid construction

Saccharomyces cerevisiae strains were created using standard yeast genetic techniques by transformation of either a PCR product (Longtine et al., 1998) or a linearized plasmid with homology regions to the yeast genome, in the BY4742 wild type strain background. Some strains with multiple genetic modifications were generated by mating, sporulation and spore selection. Plasmids were generated using standard restriction-based cloning methods. The V5 tag in the original RITE plasmid pKV015 from (Verzijlbergen et al., 2009) was replaced due to the presence of unfavourable codons that led to low expression levels of tagged proteins in yeast.

Yeast culture conditions and treatments

Yeast cultures were grown to saturation and diluted to OD=0.01 in synthetic complete medium containing 2% glucose at 30°C. Prior to induction of recombination, cells were kept and grown on selective (-Ura or hygromycin) solid or liquid medium. Exponentially growing cells were induced to recombine with 0.5 µM beta-estradiol (Sigma), and cultures were imaged in mid-exponential growth phase after the indicated times, if not mentioned otherwise. Auxin-inducible degradation of proteins was induced by treatment with 0.5 mM indole-3-acetic acid (IAA) (Sigma, I2886-5G, CAS: 87-51-4) and 4 µM phytic acid dipotassium salt (Sigma, 5681, CAS: 129832-03-7) for the indicated time.

Microscopy

Cells were imaged in 384-well plates (Matrical) coated with concanavalin A for immobilization. 3D volume stacks of yeast cells with RITE-labelled NPCs were acquired on a temperature-controlled inverted Nipkow spinning disk equipped with the Yokogawa Confocal Scanner Unit CSU-W1-T2 SoRa and a triggered Piezo z-stage (Mad City Labs Nano-Drive). It was used in spinning disk mode with a pinhole diameter of 50 µm combined with a 1.45 NA, 100x objective and controlled by the NIS Elements Software (Nikon). Images were acquired with a sCMOS Hamamatsu Orca Fusion BT camera (2304 x 2304 pixel, 6.5 x 6.5 µm pixel size). Imaging was performed at 30 °C with 50 % laser intensity of a Oxxius 488 nm 200 mW LNC Version and/or 5% laser intensity of Oxxius 561 nm 200 mW LNC Version light source. Z-stack data were taken with the Piezo stage in triggering mode with 0.2 µm sectioning. Exposure times were 200 ms for GFP and 50 ms for RFP.

NPC-tracking experiments were performed on a temperature-controlled inverted Nipkow spinning disk equipped with the Yokogawa Confocal Scanner Unit CSU-W1-T2 controlled by the VisiVIEW Software (Visitron). It was used in spinning disk mode with a pinhole diameter of 50 µm combined with a 1.45 NA, 100x objective. The microscope is equipped with two EMCCD Andor iXon Ultra cameras (1024x1024 pixel, 13x13um pixel size) and was used in a dual camera mode for measuring distances between NPCs and spindle pole bodies, in single camera mode for all tracking experiments. Imaging was performed at 30 °C with 80 % laser intensity of a DPSS 488 nm 200 mW and/or Diode 561 nm, 200 mW light source. Timelapse data were taken with 100 ms exposure time in stream mode for 300 frames. Z-stack data for Figure S1B were taken with the Piezo stage in triggering mode with 0.2 µm sectioning.

Western blotting

Logarithmically growing cells were collected and lysed with 0.1 M NaOH for 15 mins. Lysate was resuspended in SDS-loading buffer and 1 OD of cells were separated in 10 % acrylamide SDS-PAGE gels. Blotting of proteins was done with a Biorad semi-dry system in TBE buffer (pH=8.3) at 25 V and 1 Amp followed by a Ponceau-S quick protein stain. V5 epitope and Crm1 detection was performed with the following antibodies: mouse-anti-V5 antibody (AbD Serotec, MCA1360), goat-anti-mouse coupled to Alexa680 (Thermo Fisher, A-21057), rabbit-anti-Xpo1 (Zeitler & Weis, 2004) and goat-anti-rabbit coupled to IRDye800 (LI-COR Biosciences GmbH, P/N 926-32211).

Inheritance tracking

Images were acquired on the Visitron Spinning Disk microscope (see above). Cells were imaged 14 hours after RITE induction with β-estradiol at 3 min intervals in the brightfield channel to follow individual division events and identify mother-daughter pairs. At the end of the time-lapse movie, a single 3D stack was acquired in the GFP channel, and 100 mother-daughter pairs were analysed per biological replicate.

Intensity analysis of nucleolar versus non-nucleolar NE

The intensity was analysed in three biological replicates on at least 50 nuclei per condition and replicate. On maximum z-projections, nuclei in which the nucleolus presented a moon-shaped side view abutting the NE were selected manually for analysis. For each nucleus, the z-slice with the maximum intensity for the nucleolar channel (Nop1-RFP) was selected for the intensity measurement. A hand-drawn line of width 3 pixels following the NE as delineated by the Nup-GFP signal was created in FIJI first on the non-nucleolar side of the nucleus and then on the nucleolar side. Out-of-cell background was subtracted, and the ratio between the nucleolar and the non-nucleolar signal calculated.

Image and Data analysis

Image analysis and adjustments were carried out in FIJI (Schindelin et al., 2012). Data analysis, curve fitting, statistical analysis and plotting was carried out in Excel, Matlab or GraphPad Prism.

Single Particle Tracking

NPC trajectories were extracted from the movies using the FIJI (Schindelin et al., 2012) plugin Trackmate (Ershov et al., 2022). Briefly, peaks were identified using the LoG detector method with a radius of 300 nm and a quality threshold of 25. Tracks were then reconstructed from localizations using the option *simple LAP tracker* without gaps and a maximum linking distance of 300 nm. A mask based on thresholding and dilation was applied to exclude regions of high fluorescence intensity to avoid mislocalizations in regions with higher NPC densities. Additionally, tracks were filtered to have at least 5 time points, an average quality of at least 35, and a minimum quality of 25. To avoid tracks that might contain incorrectly linked localizations from one frame to the next, we also discarded tracks within 1 µm of one another. The resulting dataset was analysed using ExTrack, our probabilistic multi-state analysis pipeline (Simon et al., 2023). We used a 3-state model, since it fit the data much better than a 2-state model. For a data set of 57 tracks of 30 time points, the likelihood of the three-state model was 1.4×10^5 higher than for two states (Vaart, 1998). We extracted the diffusion coefficients of the three states for each replicate of every condition (Supplemental Figure S6B). Due to the similarity across many tested conditions, subsequent analysis used the rounded average values for the three states, 0.001 $\mu m^2/s$ (immobile state), 0.005 $\mu m^2/s$ (slow state), and 0.03 $\mu m^2/s$ (fast state), to compare the transition rates between states (Supplemental Figure S6C). These estimated transition rates were used to compute the population fractions at equilibrium (Supplemental Figure S6F). To calculate the average diffusion coefficients (Figure 6E), we computed the weighted average for each condition ($D_{avg} = F_1D_1 + F_2D_2 + F_3D_3$), where F_N is the fraction in the Nth state and D_N is the corresponding diffusion coefficient. Finally, for each individual track, we computed the probability of being in each state per timepoint (Supplemental Figure S6A).

Track simulations

To explain the differences of density between the non-nucleolar and nucleolar regions, we simulated tracks moving in an environment with two different diffusion characteristics in 2D (Figure 6A) and 3D (Figure 6D). In the 2D simulation, we characterized the impact of a change in diffusion coefficient on particle density by modelling two areas with distinct diffusion coefficients using 5000 trajectories with 5000 time steps each to find the distribution of positions at steady state. Figure 6A shows the final positions of each track. In the 3D simulations, we tested whether the observed differences in the nucleolar densities could be attributed to the differences of transition rates with the three motion states at fixed diffusion coefficients (0.001, 0.005 and 0.03 $\mu m^2/s$, Supplemental Figure S6B). Tracks were simulated on a 1 µm radius sphere composed of a body and a circular cap whose surface area was one third of the total area to represent the nucleolar region. Figure 6D shows three example tracks. In these tracks, the states switched stochastically in

time according to a Markov chain model of transition probability per step of $p_{12} = 0.028$, $p_{13} = 0$, $p_{21} = 0.013$, $p_2 = 0.041$, $p_{31} = 0$, $p_{32} = 0.15$ in the cap (nucleolus) and $p_{12} = 0.055$, $p_{13} = 0$, $p_{21} = 0.035$, $p_{23} = 0.02$, $p_{31} = 0$, $p_{32} = 0.2$ in the body (non-nucleolus). These transition probabilities were chosen based on the measured values for the *nup60*⊿ data representing the behaviour in the nucleolar territory, and the wild type data for the behaviour in the non-nucleolar territory. 1000 tracks of 2000 time steps were used to find the steady state, where the last position of each track was used to calculate the density.

To determine how the measured diffusion coefficients could be influenced by the 2D nature of our measurement of 3D diffusion, we repeated our 3D simulations for a single diffusion coefficient (Supplementary Figure S6E) and extracted the average diffusion coefficients as a function of axial position. Near the centre of the cell, that is where our experimental data is recorded, the 2D projection decreases the apparent diffusion coefficient by half (Supplementary Figure S6F). This indicates that our reported diffusion coefficients are likely an underestimate of the true values, but within a factor of two. Notably, the differences of density depend on the ratios between diffusion coefficients. As these ratios are conserved in the 2D projections, our measured densities in simulations are not affected by the shift of diffusion coefficients.

Acknowledgements

We thank Alwin Köhler for providing plasmids, ScopeM and Joachim Hehl for microscopy support, Evgeny Onischenko, Stephanie Heinrich as well as Karsten Weis and members of his group for discussion and critical comments on the manuscript. The work was supported by an ETH research grant ETH-33 19-1 to ED, and in part with funding from the Polytechnique Montréal Direction de la recherche et de l'innovation (DRI) to NK and LW, the Canada First Research Excellence Fund (TransMedTech Institute) to NK and LW and the Natural Sciences and Engineering Research Council of Canada (NSERC Discovery grant, RGPIN-2022-05142) to LW. AW acknowledges support from the Amgen Scholar Program.

Author Contributions

Conceptualization: JZ, LW and ED. Methodology: JZ, ED, FS, LW. Investigation: JZ, LI, GB, AW and ED. Formal analysis: JZ, FS, LI, LW and ED. Simulations: FS, NK and LW. Writing – Original Draft: JZ, ED. Writing – Review & Editing: all authors, Funding acquisition: LW, ED. Supervision: JZ, LW, ED.

Abbreviations

AID - auxin-inducible degron
doRITE – dilution of RITE-labelled complexes
GFP – green fluorescent protein
NE – nuclear envelope
NPC - nuclear pore complex
Nup – nucleoporin
RITE – recombination-induced tag exchange
SEM - standard error of the mean

References

Aksenova, V., Smith, A., Lee, H., Bhat, P., Esnault, C., Chen, S., Iben, J., Kaufhold, R., Yau, K. C., Echeverria, C., Fontoura, B., Arnaoutov, A., & Dasso, M. (2020). Nucleoporin TPR is an integral component of the TREX-2 mRNA export pathway. Nature Communications, 11(1). https://doi.org/10.1038/S41467-020-18266-2

Bensidoun, P., Reiter, T., Montpetit, B., Zenklusen, D., & Oeffinger, M. (2022). Nuclear mRNA metabolism drives selective basket assembly on a subset of nuclear pore complexes in budding yeast. Molecular Cell, 82(20), 3856-3871.e6. https://doi.org/10.1016/J.MOLCEL.2022.09.019

Bermejo, R., Capra, T., Jossen, R., Colosio, A., Frattini, C., Carotenuto, W., Cocito, A., Doksani, Y., Klein, H., Gómez-González, B., Aguilera, A., Katou, Y., Shirahige, K., & Foiani, M. (2011). The Replication Checkpoint Protects Fork Stability by Releasing Transcribed Genes from Nuclear Pores. Cell, 146(2), 233. https://doi.org/10.1016/J.CELL.2011.06.033

Cibulka, J., Bisaccia, F., Radisavljević, K., Carrillo, R. M. G., & Köhler, A. (2022). Assembly principle of a membrane-anchored nuclear pore basket scaffold. Science Advances, 8(6). https://doi.org/10.1126/SCIADV.ABL6863

Colombi, P., Webster, B. M., Fröhlich, F., & Lusk, C. P. (2013). The transmission of nuclear pore complexes to daughter cells requires a cytoplasmic pool of Nsp1. The Journal of Cell Biology, 203(2), 215–232. https://doi.org/10.1083/jcb.201305115

D'Angelo, M. A., & Hetzer, M. W. (2008). Structure, dynamics and function of nuclear pore complexes. In Trends in Cell Biology (Vol. 18, Issue 10, pp. 456–466). https://doi.org/10.1016/j.tcb.2008.07.009

Dilworth, D. J., Suprapto, A., Padovan, J. C., Chait, B. T., Wozniak, R. W., Rout, M. P., & Aitchison, J. D. (2001). Nup2p Dynamically Associates with the Distal Regions of the Yeast Nuclear Pore Complex. The Journal of Cell Biology, 153(7), 1465–1478. https://doi.org/10.1083/jcb.153.7.1465

Dultz, E., Wojtynek, M., Medalia, O., & Onischenko, E. (2022). The Nuclear Pore Complex: Birth, Life, and Death of a Cellular Behemoth. Cells, 11(9). https://doi.org/10.3390/CELLS11091456

Ershov, D., Phan, M. S., Pylvänäinen, J. W., Rigaud, S. U., Le Blanc, L., Charles-Orszag, A., Conway, J. R. W., Laine, R. F., Roy, N. H., Bonazzi, D., Duménil, G., Jacquemet, G., & Tinevez, J. Y. (2022). TrackMate 7: integrating state-of-the-art segmentation algorithms into tracking pipelines. Nature Methods 2022 19:7, 19(7), 829–832. https://doi.org/10.1038/s41592-022-01507-1

Feuerbach, F., Galy, V., Trelles-Sticken, E., Fromont-Racine, M., Jacquier, A., Gilson, E., Olivo-Marin, J. C., Scherthan, H., & Nehrbass, U. (2002). Nuclear architecture and spatial positioning help establish transcriptional states of telomeres in yeast. Nature Cell Biology, 4(3), 214–221. https://doi.org/10.1038/NCB756

Galy, V., Gadal, O., Fromont-Racine, M., Romano, A., Jacquier, A., & Nehrbass, U. (2004). Nuclear Retention of Unspliced mRNAs in Yeast Is Mediated by Perinuclear Mlp1. Cell, 116(1), 63–73. https://doi.org/10.1016/S0092-8674(03)01026-2

García-Benítez, F., Gaillard, H., & Aguilera, A. (2017). Physical proximity of chromatin to nuclear pores prevents harmful R loop

accumulation contributing to maintain genome stability. Proceedings of the National Academy of Sciences of the United States of America, 114(41), 10942–10947. https://doi.org/10.1073/PNAS.1707845114/SUPPL_FILE/PNAS.201707845SI.PDF

Gomar-Alba, M., Pozharskaia, V., Cichocki, B., Schaal, C., Kumar, A., Jacquel, B., Charvin, G., Igual, J. C., & Mendoza, M. (2022). Nuclear pore complex acetylation regulates mRNA export and cell cycle commitment in budding yeast. The EMBO Journal, 41(15). https://doi.org/10.15252/EMBJ.2021110271

Gunkel, P., Iino, H., Krull, S., & Cordes, V. C. (2023). An evolutionarily conserved bimodular domain anchors ZC3HC1 and its yeast homolog Pml39p to the nuclear basket. Https://Doi.Org/10.1091/Mbc.E22-09-0402. https://doi.org/10.1091/MBC.E22-09-0402

Hakhverdyan, Z., Molloy, K. R., Subbotin, R. I., Fernandez-Martinez, J., Chait, B. T., & Rout, M. P. (2021). Measuring in vivo protein turnover and exchange in yeast macromolecular assemblies. STAR Protocols, 2(3). https://doi.org/10.1016/J.XPRO.2021.100800

Heath, C. V., Copeland, C. S., Amberg, D. C., Del Priore, V., Snyder, M., & Cole, C. N. (1995). Nuclear pore complex clustering and nuclear accumulation of poly(A)+ RNA associated with mutation of the Saccharomyces cerevisiae RAT2/NUP120 gene. The Journal of Cell Biology, 131(6 Pt 2), 1677–1697. https://doi.org/10.1083/JCB.131.6.1677

Holzer, G., Magistris, P. De, Gramminger, C., Sachdev, R., Magalska, A., Schooley, A., Scheufen, A., Lennartz, B., Tatarek-Nossol, M., Lue, H., Linder, M. I., Kutay, U., Preisinger, C., Moreno-Andres, D., & Antonin, W. (2021). The nucleoporin Nup50 activates the Ran guanine nucleotide exchange factor RCC1 to promote NPC assembly at the end of mitosis. The EMBO Journal, 40(23), e108788. https://doi.org/10.15252/EMBJ.2021108788

Ishii, K., Arib, G., Lin, C., Van Houwe, G., & Laemmli, U. K. (2002). Chromatin boundaries in budding yeast: The nuclear pore connection. Cell, 109(5), 551–562. https://doi.org/10.1016/S0092-8674(02)00756-0

Khmelinskii, A., Keller, P. J., Lorenz, H., Schiebel, E., & Knop, M. (2010). Segregation of yeast nuclear pores. In Nature (Vol. 466, Issue 7305, pp. E1–E1). Nature Publishing Group. https://doi.org/10.1038/nature09255

King, G. A., Wettstein, R., Varberg, J. M., Chetlapalli, K., Walsh, M. E., Gillet, L. C. J., Hernández-Armenta, C., Beltrao, P., Aebersold, R., Jaspersen, S. L., Matos, J., & Ünal, E. (2023). Meiotic nuclear pore complex remodeling provides key insights into nuclear basket organization. The Journal of Cell Biology, 222(2). https://doi.org/10.1083/jcb.202204039

Kumar, S., Neal, M. L., Li, S., Navare, A. T., Van Eeuwen, T., Wozniak, R. W., Mast, F. D., Rout, M. P., & Aitchison, J. D. (2023). Nuclear pore complexes mediate subtelomeric gene silencing by regulating PCNA levels on chromatin. The Journal of Cell Biology, 222(9). https://doi.org/10.1083/JCB.202207060/214189

Longtine, M. S., Mckenzie III, A., Demarini, D. J., Shah, N. G., Wach, A., Brachat, A., Philippsen, P., & Pringle, J. R. (1998). Additional modules for versatile and economical PCR-based gene deletion and modification in Saccharomyces cerevisiae. Yeast, 14(10), 953–961. https://doi.org/10.1002/(sici)1097-0061(199807)14:10<953::aid-yea293>3.3.co;2-l

Lusk, C. P., & Colombi, P. (2014). Toward a consensus on the mechanism of nuclear pore complex inheritance. Nucleus, 5(2), 97–102. https://doi.org/10.4161/NUCL.28314

Markossian, S., Suresh, S., Osmani, A. H., & Osmani, S. A. (2015). Nup2 requires a highly divergent partner, NupA, to fulfill functions at nuclear pore complexes and the mitotic chromatin region. Molecular Biology of the Cell, 26(4), 605. https://doi.org/10.1091/MBC.E14-09-1359

Meinema, A. C., Marzelliusardottir, A., Mirkovic, M., Aspert, T., Lee, S. S., Charvin, G., & Barral, Y. (2022). DNA circles promote yeast ageing in part through stimulating the reorganization of nuclear pore complexes. ELife, 11. https://doi.org/10.7554/ELIFE.71196

Niepel, M., Molloy, K. R., Williams, R., Farrc, J. C., Meinema, A. C., Vecchietti, N., Cristea, I. M., Chait, B. T., Rout, M. P., & Strambio-De-Castillia, C. (2013). The nuclear basket proteins Mlp1p and Mlp2p are part of a dynamic interactome including Esc1p and the proteasome. Molecular Biology of the Cell, 24(24), 3920. https://doi.org/10.1091/MBC.E13-07-0412

Niepel, M., Strambio-de-Castillia, C., Fasolo, J., Chait, B. T., & Rout, M. P. (2005). The nuclear pore complex-associated protein, Mlp2p, binds to the yeast spindle pole body and promotes its efficient assembly. The Journal of Cell Biology, 170(2), 225–235. https://doi.org/10.1083/JCB.200504140

Nishimura, K., Fukagawa, T., Takisawa, H., Kakimoto, T., & Kanemaki, M. (2009). An auxin-based degron system for the rapid depletion of proteins in nonplant cells. Nature Methods, 6(12), 917–922. https://doi.org/10.1038/NMETH.1401

Nordeen, S. A., Turman, D. L., & Schwartz, T. U. (2020). Yeast Nup84-Nup133 complex structure details flexibility and reveals conservation of the membrane anchoring ALPS motif. Nature Communications, 11(1), 1–12. https://doi.org/10.1038/s41467-020-19885-5

Onischenko, E., Noor, E., Fischer, J. S., Gillet, L., Wojtynek, M., Vallotton, P., & Weis, K. (2020). Maturation Kinetics of a Multiprotein Complex Revealed by Metabolic Labeling. Cell, 183(7), 1785-1800.e26. https://doi.org/10.1016/J.CELL.2020.11.001

Palancade, B., Liu, X., Garcia-Rubio, M., Aguilera, A., Zhao, X., & Doye, V. (2007). Nucleoporins prevent DNA damage accumulation by modulating Ulp1-dependent sumoylation processes. Molecular Biology of the Cell, 18(8), 2912–2923. https://doi.org/10.1091/MBC.E07-02-0123

Palancade, B., Zuccolo, M., Loeillet, S., Nicolas, A., & Doye, V. (2005). Pml39, a Novel Protein of the Nuclear Periphery Required for Nuclear Retention of Improper Messenger Ribonucleoparticles. Molecular Biology of the Cell, 16(11), 5258–5268. https://doi.org/10.1091/mbc.e05-06-0527

Patrizia Derrer, C., Mancini, R., Vallotton, P., Huet, S., Weis, K., & Dultz, E. (2019). The RNA export factor Mex67 functions as a mobile nucleoporin. https://doi.org/10.1083/jcb.201909028

Rabut, G., Doye, V., & Ellenberg, J. (2004). Mapping the dynamic organization of the nuclear pore complex inside single living cells. Nature Cell Biology, 6(11), 1114–1121. https://doi.org/10.1038/ncb1184

Saroufim, M. A., Bensidoun, P., Raymond, P., Rahman, S., Krause, M. R., Oeffinger, M., & Zenklusen, D. (2015). The nuclear basket mediates perinuclear mRNA scanning in budding yeast. The Journal of Cell Biology, 211(6), 1131–1140. https://doi.org/10.1083/JCB.201503070

Savas, J. N., Toyama, B. H., Xu, T., Yates, J. R., & Hetzer, M. W. (2012). Extremely long-lived nuclear pore proteins in the rat brain. Science (New York, N.Y.), 335(6071), 942. https://doi.org/10.1126/SCIENCE.1217421

Schindelin, J., Arganda-Carreras, I., Frise, E., Kaynig, V., Longair, M., Pietzsch, T., Preibisch, S., Rueden, C., Saalfeld, S., Schmid, B., Tinevez, J. Y., White, D. J., Hartenstein, V., Eliceiri, K., Tomancak, P., & Cardona, A. (2012). Fiji: An open-source platform for biological-image analysis. In Nature Methods (Vol. 9, Issue 7, pp. 676–682). https://doi.org/10.1038/nmeth.2019

Simon, F., Tinevez, J. Y., & van Teeffelen, S. (2023). ExTrack characterizes transition kinetics and diffusion in noisy single-particle tracks. The Journal of Cell Biology, 222(5). https://doi.org/10.1083/JCB.202208059

Spichal, M., Brion, A., Herbert, S., Cournac, A., Marbouty, M., Zimmer, C., Koszul, R., & Fabre, E. (2016). Evidence for a dual role of actin in regulating chromosome organization and dynamics in yeast. Journal of Cell Science, 129(4), 681–692. https://doi.org/10.1242/jcs.175745

Strambio-de-Castillia, C., Blobel, G., & Rout, M. P. (1999). Proteins connecting the nuclear pore complex with the nuclear interior. The Journal of Cell Biology, 144(5), 839–855. https://doi.org/10.1083/JCB.144.5.839

Sumner, M. C., & Brickner, J. (2022). The Nuclear Pore Complex as a Transcription Regulator. Cold Spring Harbor Perspectives in Biology, 14(1). https://doi.org/10.1101/CSHPERSPECT.A039438

Tartakoff, A., DiMario, P., Hurt, E., McStay, B., Panse, V. G., & Tollervey, D. (2022). The dual nature of the nucleolus. Genes & Development, 36(13–14), 765. https://doi.org/10.1101/GAD.349748.122

Toyama, B. H., Drigo, R. A., Lev-Ram, V., Ramachandra, R., Deerinck, T. J., Lechene, C., Ellisman, M. H., & Hetzer, M. W. (2019). Visualization of long-lived proteins reveals age mosaicism within nuclei of postmitotic cells. Journal of Cell Biology, 218(2), 433–444. https://doi.org/10.1083/jcb.201809123

Vaart, A. W. van der. (1998). Asymptotic Statistics. Asymptotic Statistics. https://doi.org/10.1017/CBO9780511802256

Verzijlbergen, K. F., Menendez-Benito, V., van Welsem, T., van Deventer, S. J., Lindstrom, D. L., Ovaa, H., Neefjes, J., Gottschling, D. E., & van Leeuwen, F. (2009). Recombination-induced tag exchange to track old and new proteins. Proceedings of the National Academy of Sciences, 107(1), 64–68. https://doi.org/10.1073/pnas.0911164107

Wang, R., Kamgoue, A., Normand, C., Léger-Silvestre, I., Mangeat, T., & Gadal, O. (2016). High resolution microscopy reveals the nuclear shape of budding yeast during cell cycle and in various biological states. Journal of Cell Science, 129(24), 4480–4495. https://doi.org/10.1242/JCS.188250

Winey, M., Yarar, D., Giddings, T. H., & Mastronarde, D. N. (1997). Nuclear pore complex number and distribution throughout the Saccharomyces cerevisiae cell cycle by three-dimensional reconstruction from electron micrographs of nuclear envelopes. Molecular Biology of the Cell, 8(11), 2119–2132. https://doi.org/10.1091/MBC.8.11.2119

Zeitler, B., & Weis, K. (2004). The FG-repeat asymmetry of the nuclear pore complex is dispensable for bulk nucleocytoplasmic transport in vivo. The Journal of Cell Biology, 167(4), 583–590. https://doi.org/10.1083/JCB.200407156

Supplemental Figures

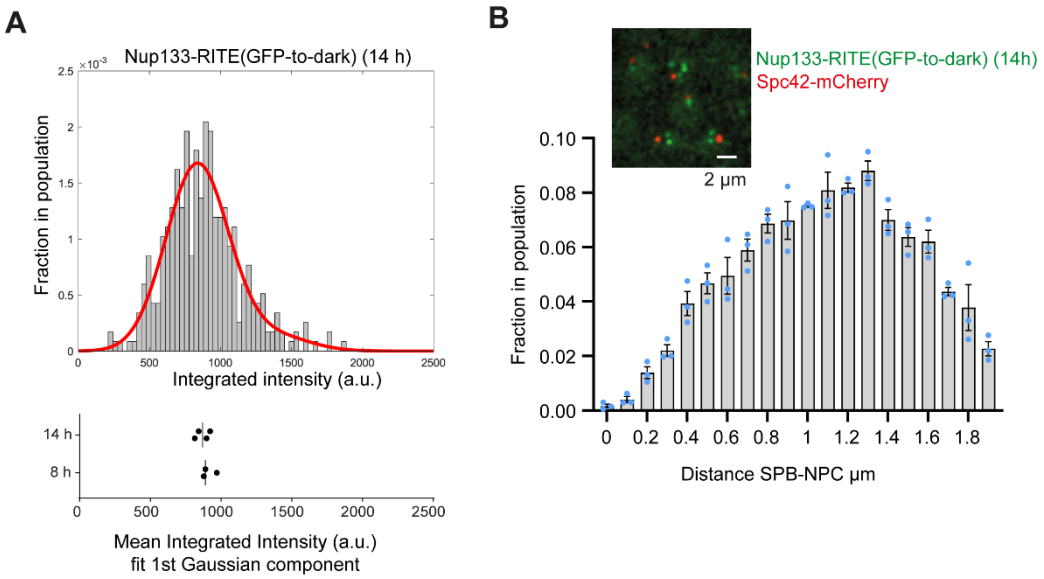

Figure S1: doRITE foci show the characteristics of individual NPCs. (A) Recombination of exponentially growing cells expressing Nup133-RITE(GFP-to-dark) were induced for 8 or 14 h, 3D stacks were acquired and integrated intensity of individual fluorescent foci was quantified. Top: Intensity distribution of 350 isolated foci. The red line represents a 2-component Gaussian fit. Bottom: Dots are the centre peak position of the smaller component of the Gaussian fit for replicates of NPC intensity distributions 8 or 14 hours after RITE induction. Lines represent median. Each distribution contains >200 individual foci. **(B)** Distribution of distances of Nup133-RITE(GFP-to-dark) foci at 14 h after RITE induction from the spindle pole body (SPB) labelled by Spc42-mCherry. At least 500 SPB-NPC distances were measured per replicate. Blue dots represent fraction in individual biological replicates. Error bars represent standard error of the mean. Image shows a representative maximum projection of the analysed cells.

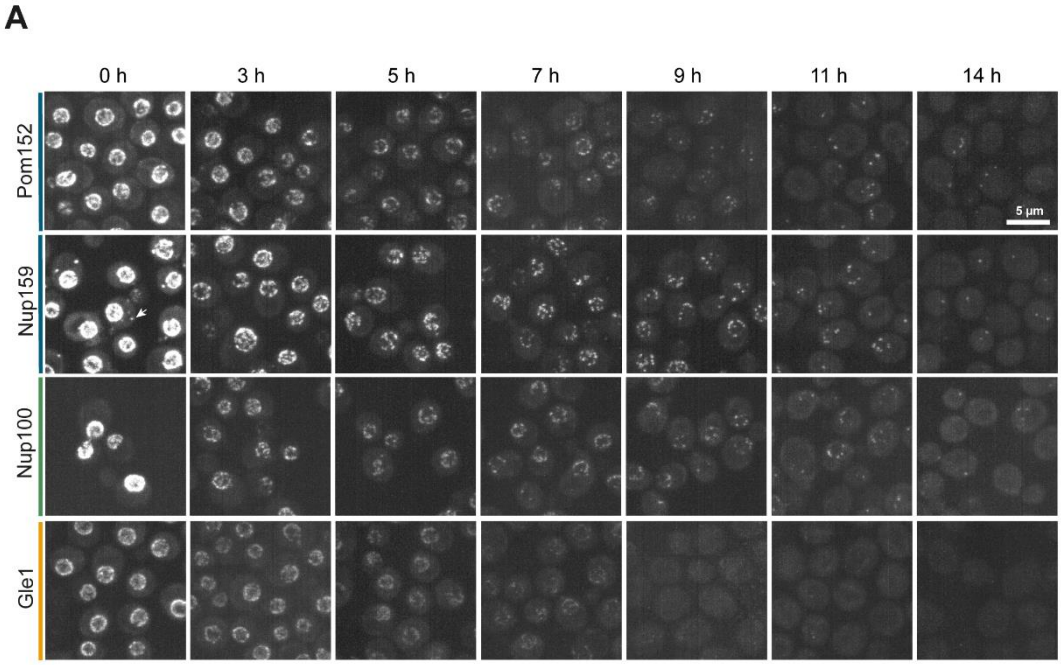

Figure S2: Nup dynamics determined by doRITE. (A) Exponentially growing cells expressing the indicated Nups tagged with a GFP-to-dark RITE cassette. Time stamps specify time after induction of RITE. Maximum projections are shown. Colour bars represent membership to dynamic group in Figure 2A.

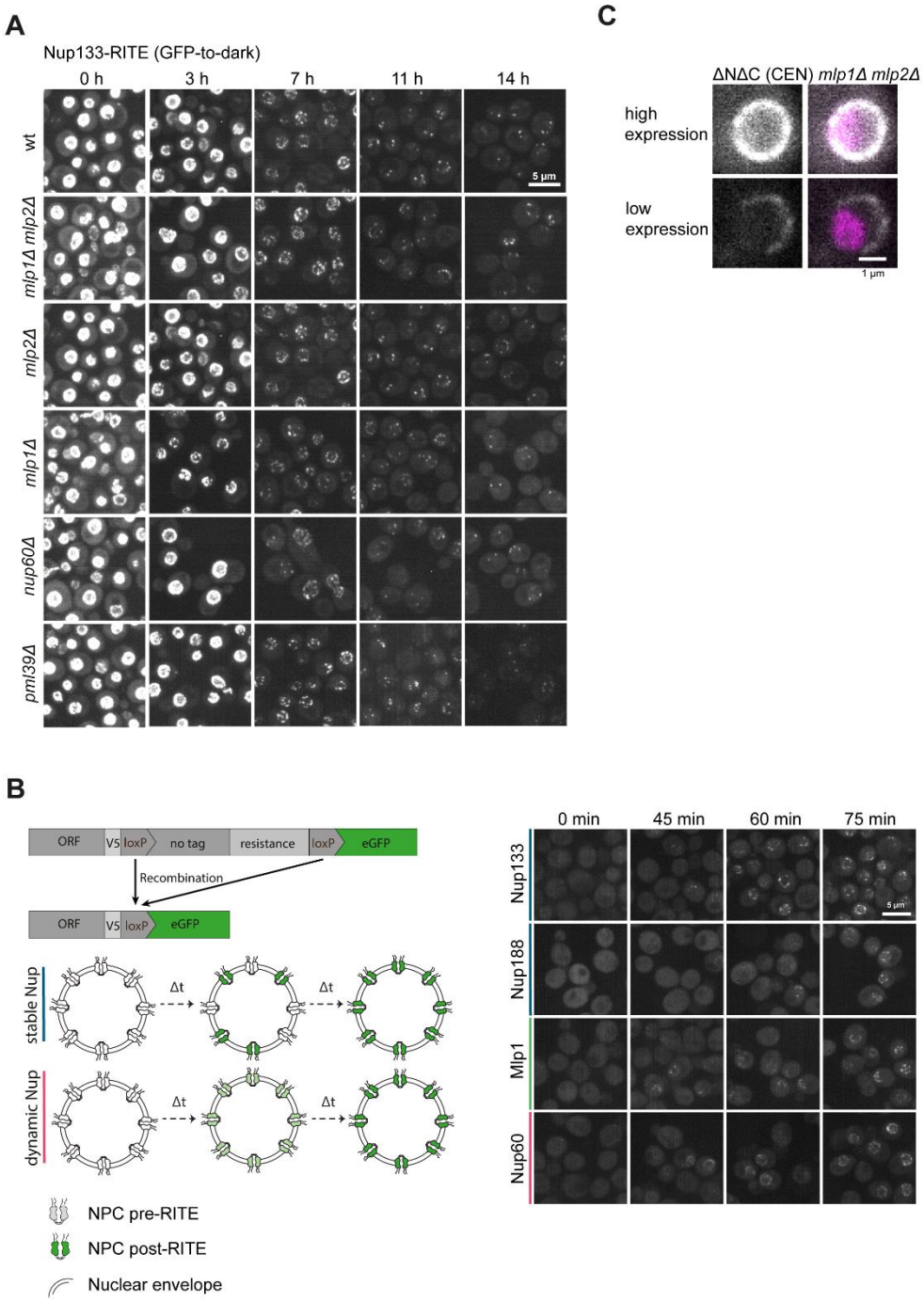

Figure S3: Exclusion of old NPCs from the nucleolar territory depends on Mlp1. (A) Exponentially growing cells expressing Nup133-RITE (GFP-to-dark) and carrying deletions in different nuclear basket Nups. Time stamps specify the time after induction of RITE. Maximum projections are shown. **(B)** Left: Schematic of RITE cassette to visualize new proteins (newRITE). Appearance of newly synthesized NPCs, when a stable or dynamic Nup is tagged. Right: Exponentially growing cells expressing the indicated Nups tagged with a dark-to-GFP RITE cassette. Time stamps specify time after induction of RITE. Maximum projections are shown. **(C)** Exponentially growing cells overexpressing Mlp1ΔNΔC-GFP fragment from a CEN plasmid in the absence of endogenous Mlp1 and Mlp2. Panel shows 2 nuclei with the nucleolus marked by Nop1-RFP. While most cells exhibit low expression and nucleolar exclusion of the fragment, some cells display high expression and a more homogenous NE staining.

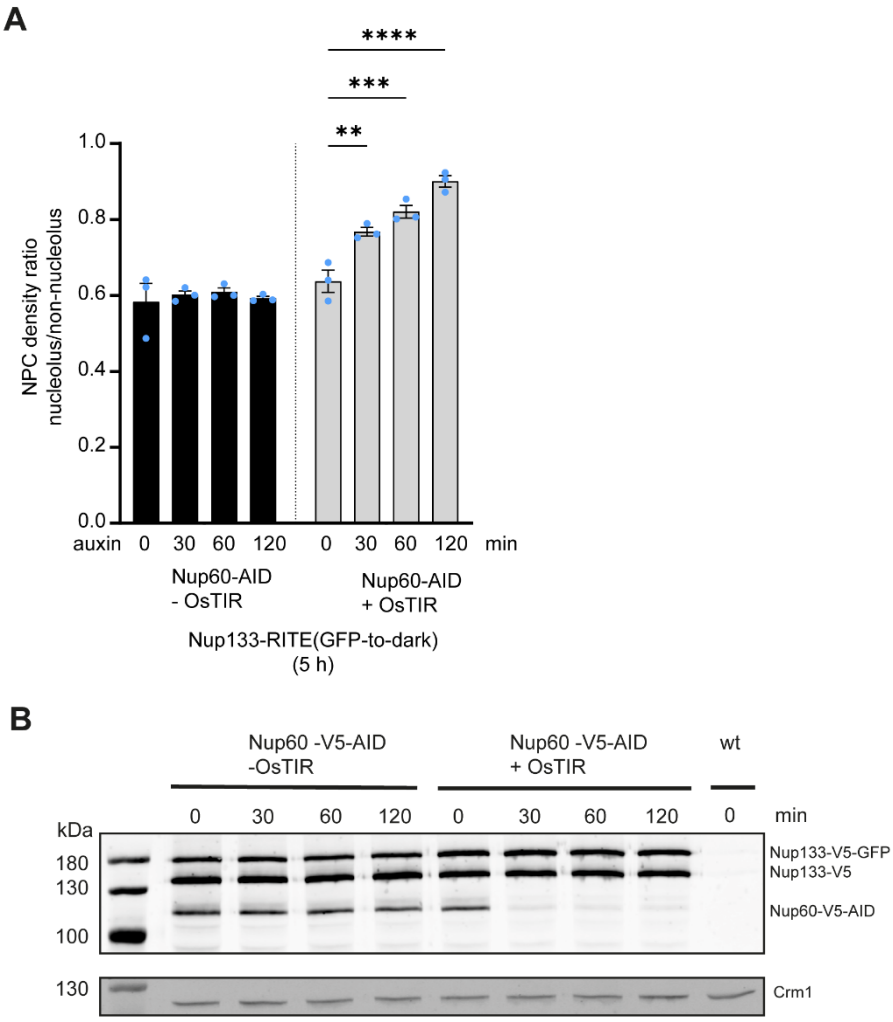

Figure S4: NPC density in the nucleolar territory increases upon depletion of Nup60. (A) Exponentially growing cells expressing Nup133-RITE(GFP-to-dark) and Nup60 tagged with the auxin inducible degron were induced with auxin for the indicated times either in the absence or presence of the E3 ligase OsTIRr1. Ratio of nucleolar to non-nucleolar Nup133-RITE(GFP-to-dark) signal was quantified after 5 hours of RITE induction and acute depletion of Nup60. Blue dots show the average of biological replicates and error bars show the standard error of the mean. Star indicates significance in one-way ANOVA with Sidak multiple comparison correction: ** $p<0.005$, *** $p<0.001$ **** $p<0.0001$. At least 50 cells were analyzed per replicate and condition. **(B)** Western blot of the depletion of Nup60 by an auxin inducible degron (AID). V5 antibody detects both the Nup60-AID as well as the RITE-tagged Nup133, spontaneous recombination is visible by the shift to a lower molecular size of Nup133-V5 signal as cells were not grown under selection for the RITE cassette. Crm1 was used as a loading control.

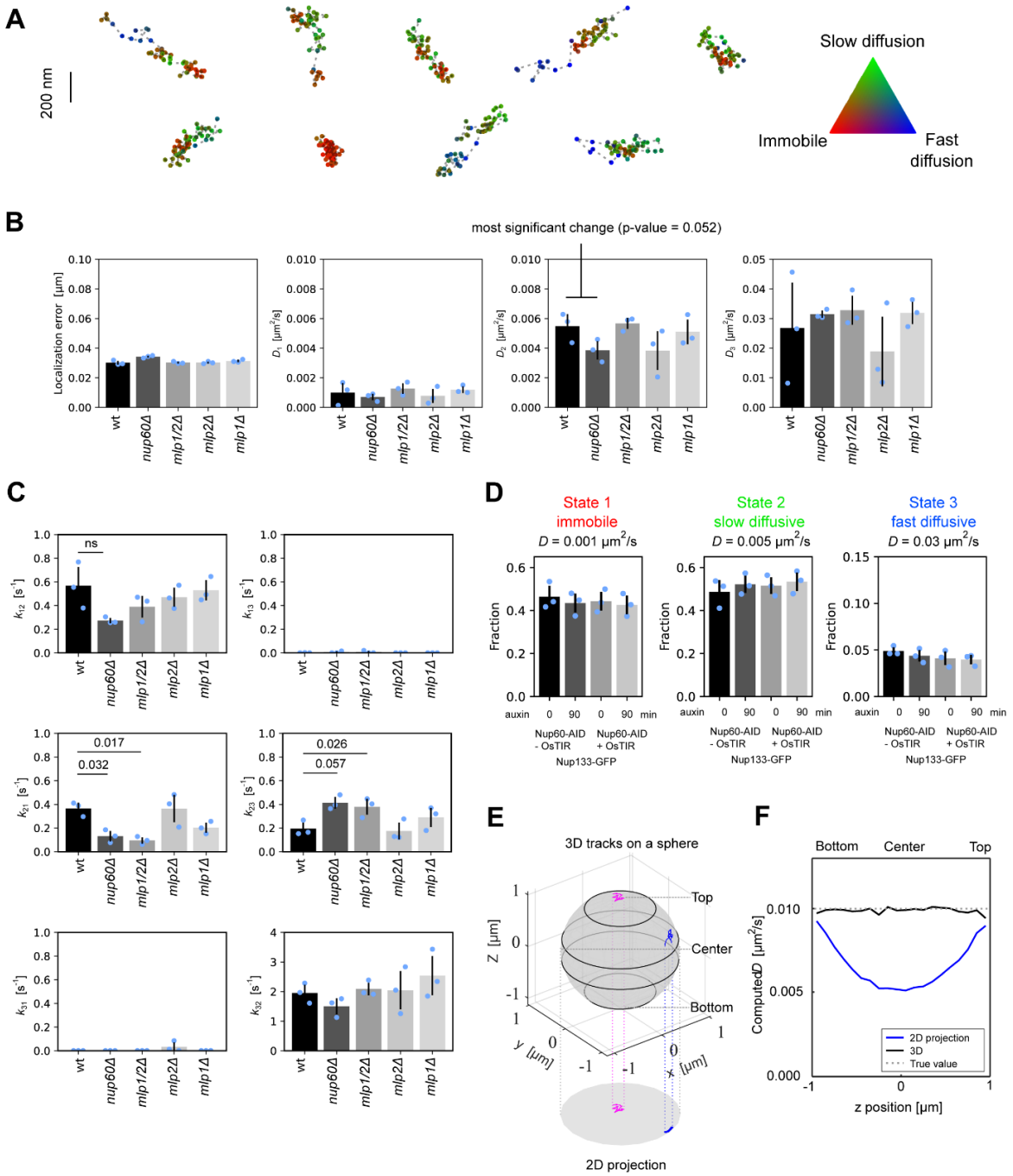

Figure S5: The nuclear basket proteins influence the mobility of NPCs. being in a specific state at each time-point. (A) Example NPC trajectories from the WT strain. The ternary colour plot shows the probability of being in a specific state at each time-point. **(B)** A 3-state model was fit to tracks obtained from labelled NPCs in exponentially growing cells expressing Nup133-RITE(GFP-to-old) 14 hours after induction. Bar graphs show the obtained localization error estimates and diffusion coefficients estimated for the different mutants. The localization errors and diffusion coefficients did not differ significantly between the different strains. Results from individual biological replicates are shown as blue dots, the error bars represent the standard deviation of three biological replicates. At least 1100 tracks were analysed per condition and replicate. P value is from pairwise t-test. **(C)** A 3-state model with fixed diffusion coefficients (D_1 = 0.001 µm²/s, D_2 = 0.005 µm²/s, D_3 = 0.03 µm²/s) was fit to the same data as in (B). Transition rates between the different states are shown. Error bars represent the standard deviation. P-values are from pairwise t-tests. All other pair-wise comparisons were not significant. Transition rates shown here were used to compute fractions in different states shown in Figure 5B. **(D)** A 3-state model with fixed diffusion coefficients (D_1 = 0.001 µm²/s, D_2 = 0.005 µm²/s, D_3 = 0.03 µm²/s) was fit to tracks obtained from Nup133-RITE(GFP-to-old) labelled NPCs expressing Nup60 tagged with an auxin-inducible degron 14 hours after RITE induction. Nup60 degradation was induced with auxin for 90 min. Degradation occurred in strains carrying the OsTIR1-E3 ligase. Bar graphs display the fraction of particles in each diffusive state. Results from individual biological replicates are shown as blue dots, the error bars represent the standard deviation. By pairwise t-test, results did not differ between conditions with or without Nup60. At least 1500 tracks were analysed per condition and replicate. **(E)** Illustration demonstrating the projection of 3D tracks onto a 2D plane. The axes are in µm and the sphere diameter is 2 µm. **(F)** Quantification of the measured diffusion coefficients from 3D and from projected 2D trajectories. We simulated 200,000 tracks with 11 timesteps moving on a sphere with a diffusion coefficient of 0.01 µm²/s. The apparent diffusion coefficient of each track was computed by fitting a first-order polynomial to its mean squared displacements (MSD). Then, tracks were binned according to their mean z position and the average apparent diffusion coefficient were computed for each bin.